Atmos. Meas. Tech., 19, 2149–2161, 2026
https://doi.org/10.5194/amt-19-2149-2026

Atmospheric Measurement Techniques
Open Access
EGU

Lidar measurement of aircraft engine particulate emissions

Romain Ceolato[1], Andrés Bedoya-Velásquez[1], Gerald Lemineur[1], Pierrick Loyers[2], Charles Renard[2], Katharina Seeliger[2], Louise Ganeau[3], Alaric Vandestoc[3], Ismael Ortega[3], Mark Johnson[4], and David Delhaye[5]

[1]ONERA, Université de Toulouse, Toulouse, France
[2]Airbus Operations SAS, Toulouse, France
[3]ONERA, Paris-Saclay University, 91123 Palaiseau, France
[4]Rolls-Royce plc, Derby, United Kingdom
[5]DGAC French Civil Aviation Authority, Paris, France

Correspondence: Romain Ceolato (romain.ceolato@onera.fr)

Received: 13 June 2025 – Discussion started: 7 August 2025
Revised: 11 October 2025 – Accepted: 10 December 2025 – Published: 30 March 2026

Abstract. Particulate matter (PM) emitted by aircraft engines represents a major non-CO_2 emission source, primarily composed of soot particles generated by incomplete fuel combustion. These particles act as ice nuclei in contrail formation and degrade air quality near airports. A novel technique is introduced to investigate aircraft engine PM emissions using a short-range elastic backscattering lidar. This approach was validated through trials conducted at the Airbus Bikini test site using the compact and field-deployable Colibri Aerosol Lidar (CAL) sensor. This instrument enables rapid, non-invasive, and remote measurement of volume backscatter profiles, which can be converted into PM mass and number concentrations without the need to sample particles from the aircraft exhaust. Our findings demonstrate the feasibility and potential of using a short-range elastic backscattering lidar for remote assessment of aircraft PM emissions across various engine thrust levels.

1 Introduction

Quantifying non-CO_2 emissions from aircraft engines, particularly non-volatile particulate matter (nvPM) or soot particles, has become a critical focus in aviation environmental research (Lee et al., 2023; Aamaas et al., 2025). These emissions impact local air quality around airports and contribute to the formation of contrails and contrail-induced cirrus clouds, which may influence the global Earth's radiative balance by altering light absorption and scattering in the stratosphere (Yu et al., 2024; Klöwer et al., 2021). Regulatory standards, such as those established by the International Civil Aviation Organization (ICAO, 2017), are also driving industry efforts to reduce PM emissions from aircraft engines including technological advances in engine design, the use of low-sulfur jet fuel, and improved combustion efficiency. The PM emissions at the aircraft turbine engine exit plane consist mainly of nonvolatile Particulate Matter (nvPM), or black carbon soot, while other constituents, such as volatile Particulate Matter (vPM), may be formed downstream as the exhaust plume dilutes and cools in the atmosphere. These vPM are comprised primarily of sulfur and organic compounds and generally do not form until the exhaust plume has sufficiently diluted and cooled in the atmosphere downstream of the engine (Jones and Miake-Lye, 2024). nvPM is defined as solid particles formed during the combustion process, typically with diameters between 10 and 100 nm, which are present at the engine exit plane and do not volatilize when heated to 350 °C (SAE International, 2018, 2019). Therefore, there has been a growing need to monitor nvPM emissions from aircraft to better understand their composition and formation mechanisms, to mitigate their environmental and health effects. In the context of aircraft engine emissions, nvPM consists exclusively of soot particles; thus, in this study, the terms nvPM and soot are used interchangeably.

Measuring nvPM emissions from aircraft engines is challenging due to the complex nature of exhaust plumes, which involve high temperatures, high velocities, and rapid dilution in the atmosphere. Engine certification procedure for measur-

ing nvPM concentrations has evolved recently, going from the measurement of smoke number to the measurement of nvPM number and mass concentration (ICAO, 2017). Certification measurements require sample dilution and long lines (up to 32 m), leading to significant uncertainties, especially in line loss corrections, and making it hard to estimate engine exit plane values (Durand et al., 2023). Because of these challenges and the need for loss correction methods, new techniques have been developed to measure nvPM emissions from aircraft engines. These techniques include laser or active remote-sensing methods, such as elastic backscatter lidar (EBL), which can provide information about the presence, distribution, and relative concentration of a wide range of atmospheric aerosols, including soot particles.

Recent advancements have brought the use of lidar techniques closer to new applications involving in situ instruments. In particular, Short-Range Elastic Backscatter Lidar (SR-EBL) techniques have proven to be able to probe the mass and number concentration of black carbon aerosols in the first tens of meters, unlike traditional long-range atmospheric lidars. SR-EBL sensors have demonstrated the ability to provide precise and non-invasive characterization of particulate matter near ground level, in synergy with in situ instruments for monitoring urban air pollution and traffic-related emissions (Bedoya-Velásquez et al., 2024). These emerging lidar techniques may offer an alternative to conventional in situ sampling methods for assessing nvPM concentrations, such as aircraft gas engines.

Here, we introduce a novel approach for directly measuring nvPM from an aircraft engine using a short-range aerosol lidar. First, the sensor and associated retrieval methodology are described. Subsequently, measurements are presented to demonstrate the feasibility and potential of this technique for monitoring on-wing engine particulate emissions. Our novel sensor is designed to offer a rapid, precise, and efficient characterization of soot emissions, while overcoming the limitations associated with in situ sensors. The development of this sensor represents a step forward in the monitoring of non-CO2 aircraft emissions, contributing to efforts to mitigate the environmental impact of the aviation sector.

2 Materials and methods

2.1 Principle of measurement

In this section, an overview of the principle of the backscatter lidar-based technique is provided. The principle of operation has been described in further detail in previous work (Ceolato and Berg, 2021). Briefly, the short-range elastic backscatter lidar (SR-EBL) consists in using the Time-of-Flight (ToF) method to measure the range-resolved backscattering intensity, enhancing the signal-to-noise ratio (SNR). By applying temporal filtering or gating, it effectively suppresses background noise, offering a clear advantage over conventional optical techniques (e.g. spectroscopy or imaging). The raw lidar signal $S(r)$ directly depends on the volume of illuminated particulate matter, located at a distance r from the sensor. It is a common practice to use the range-corrected signals RCS instead of the lidar signal to remove the range dependence on the signal, such as:

$$\mathrm{RCS}(r) = S(r)r^2 = K_\mathrm{o}(r)U(r) \ \ [\mathrm{V\,m^2}], \tag{1}$$

where $K_\mathrm{o}(r)$ is the lidar constant, directly derived from the radiometric lidar constant, which depends on several parameters such as the laser pulse energy or the sensor gain and sensitivity, and the overlap or geometric function. We note that the lidar calibration constant changes from instrument to instrument because of the variation in laser, optical loss, and sensor response. The elastic lidar equation provides a simple expression of the attenuated backscatter profiles $U(r)$ under the single-scattering approximation (SSA) (Measures, 1984; Ceolato and Berg, 2021), i.e.

$$U(r) = \beta(r)T(r) \ \text{ where } \ T(r) = \exp\left(-2\int_0^r \alpha\left(r'\right)\mathrm{d}r'\right), \tag{2}$$

where $\alpha(r)$ and $\beta(r)$ are the range-dependent *volume* extinction and backscattering coefficients, with units of $[\mathrm{m^{-1}}]$ and $[\mathrm{m^{-1}\,sr^{-1}}]$, respectively.

For optically thin combustion plumes such as aircraft exhaust plumes, i.e. $T(r) \sim 1$, the volume backscattering coefficient $\beta(r)$ is approximately equal to the attenuated backscattering coefficient $U(r)$. Thus, Eq. (1) becomes,

$$\mathrm{RCS}(r) = K_\mathrm{o}(r)\beta(r) \ \ [\mathrm{V\,m^2}]. \tag{3}$$

All optical instruments, including in situ and remote sensing techniques, rely on having the appropriate optical model to invert raw electrical signals into useful information. For instance, Laser Induced Incandescence (LII) requires a solid knowledge of soot refractive index to infer absorption efficiency and retrieve mass concentration information. Absorption instruments such as the Photoacoustic Extinctiometer (PAX) or extinction instruments such as the Cavity Attenuated Phase Shift (CAPS) measure the aerosol absorption and extinction coefficients, respectively. Soot mass concentrations can then be inferred from these optical measurements using appropriate mass absorption (MAC) or mass extinction coefficients (MEC) (Liu et al., 2020; Smith et al., 2015). Here, SR-EBL relies on the backscattering properties of soot particles. Among these properties, two main parameters are needed to invert the SR-EBL signals into number and mass concentrations: the differential backscattering cross-section $\mathrm{d}C^{\mathrm{bac}}$ and the mass-backscattering coefficient (MBC), respectively. The volume backscattering coefficients can be converted to soot number and mass concentrations by dividing them by a reference coefficient.

The range-dependent particle number concentration $n_o(r)$ is directly related to the volume backscattering coefficient,

$$n_o(r) = \frac{\beta(r)}{dC^{bac}}, \tag{4}$$

where dC^{bac} is the mean differential backscattering cross-section, with units of $[m^2\,sr^{-1}]$, defined as,

$$dC^{bac} = \overline{dC^{bac}} = \int_{R_{min}}^{R_{max}} p(R) dC^{bac}(R)\,dR, \tag{5}$$

where $p(R)$ is the normalized probability density function describing the aerosol radius distribution. Here, the soot aerosols are assumed to constitute an isotropic scattering medium consisting of a log-normal ensemble of randomly oriented particles with a mean geometric radius R. The radii R_{min} and R_{max} in Eq. (5) denote the minimum and maximum geometric mean radii, respectively. The differential backscattering cross section dC^{bac} can, in general, be obtained from the Stokes phase matrix (Mishchenko et al., 2002).

Similarly, the range-dependent particle mass concentration $m_o(r)$ is directly related to the volume backscattering coefficient,

$$m_o(r) = \frac{\beta(r)}{MBC}, \tag{6}$$

where MBC, with units of $[m^2\,g^{-1}\,sr^{-1}]$, is defined as the ratio

$$MBC = \frac{dC^{bac}_{soot}}{m_{soot}} = \frac{dC^{bac}_{soot}}{\rho_{eff}} V_{soot}, \tag{7}$$

where m_{soot} is the mass of a soot particle and ρ_{eff} is the effective soot density with units $[kg\,m^{-3}]$. This coefficient, also called the specific mass backscattering coefficient, is essential to convert lidar signals into mass concentration. It can be seen as the backscattering analogue of the MAC or MEC used by other traditional optical techniques.

Consequently, the retrieval of physical quantities from lidar measurements relies on the use of appropriate optical properties. It is important to note that the performance of the SR-EBL in measuring particle number and mass concentrations depends on knowledge of the optical properties of particulate matter. This information can be obtained through laboratory calibration or by employing a suitable aerosol optical model. In this study, the latter approach was adopted, based on state-of-the-art knowledge of aircraft soot particles, and will be detailed in the following sections.

2.2 Optical model for aircraft engine particulate matter

Modeling backscattering properties is particularly challenging for soot particles, which are highly absorbing and have complex optical properties, and has been investigated in previous studies (Kanngiesser and Kahnert, 2019; Liu and Mishchenko, 2020). Numerical calculations of the radiative properties of soot have been developed using various light-scattering theories: ranging from Lorenz–Mie theory, which assumes a spherical shape and symmetry, to more advanced approaches such as the T-Matrix and Discrete Dipole Approximation (DDA) methods, which account for more complex morphologies (Qin et al., 2024; Ishimoto et al., 2019). These methods offer varying levels of accuracy for applications in atmospheric science, combustion diagnostics, and climate research.

A backscattering model based on the Rayleigh-Debye-Gans for Fractal Aggregates (RDG-FA) has been proposed to model the lidar parameters of soot particles, accounting for their fractal morphology (Ceolato et al., 2025). This model is a light-scattering approximation for fractal aggregates, based on two assumptions: monomers scatter light independently, and the phase shift across each monomer is negligible. Its accuracy depends on parameters such as monomer size, fractal dimension, wavelength, and refractive index, and has been extensively discussed in previous works (Sorensen, 2001). These assumptions hold for soot particles with small aggregates composed of small monomers, which are typically found in aircraft particulate matter emissions. Despite its simplicity, RDG-FA shows good agreement with experimental light-scattering data for soot, especially when averaged over random aggregate orientations, and has been recently introduced for lidar inversion. This model was successfully used for retrieving the number and mass concentrations of kerosene combustion-derived soot emitted from a turbulent small-scale pool fire (Ceolato et al., 2022).

Subsequently, we will model the aircraft engine particulate matter as soot fractal aggregates (Teoh et al., 2019). Such aggregates are considered fractal if they display self-similarity across their size scales, that relates aggregate mass or number of monomers N, and follows the classic *fractal scaling law*,

$$N = k_o \left(\frac{D_g}{D_m} \right)^{D_f}, \tag{8}$$

where the fractal dimension D_f characterizes the overall morphology of the aggregates and the fractal prefactor k_o represents a degree of compactness of the aggregate. In addition to these morphological parameters, the size of the particles is expressed in terms of the monomer diameter, D_m, and the diameter of gyration, D_g, which represents the diameter of a sphere with the same moment of inertia as an aggregate with N monomers. Here, the proposed values of the soot fractal aggregate model for aircraft particulate matter are based on the following parameters: $D_f = 1.9$, $k_o = 2.3$, $D_m = 20\,nm$, and $D_g = 50\,nm$. These values are typically obtained from imaging techniques such as transmission electron microscopy (TEM), as reported in the literature (Delhaye et al., 2017; Marhaba et al., 2019). Furthermore, the

ratio $X_R = D_m/D_g = 0.4$ is consistent with the median value derived from measurements and used to model soot particle (Kumal et al., 2020; Yu et al., 2024). However, significant uncertainties remain regarding the nvPM morphological properties of modern engines such as the TXWB-84. This gap highlights the need for further research and comprehensive measurements. The selection of an appropriate complex refractive index for soot remains debated due to the complex and interrelated uncertainties involved (Digby et al., 2025). The recently recommended value of $m = 1.95 + 0.96i$ for freshly emitted black carbon (Moteki et al., 2023) is used here and corresponds to a low organic carbon to total carbon ratio (OC / TC), as reported for most aircraft engine thrusts (Marhaba et al., 2019; Trivanovic et al., 2022). Another key parameter is the effective mass density for particulate matter, commonly assumed to be $\rho = 1000\,\mathrm{kg\,m^{-3}}$ in aircraft particulate studies (ICAO, 2017; Durdina et al., 2014). More complex and size-resolved effective density models have been developed, but this value has been shown to give accurate results for a wide range of engine thrusts (Durdina et al., 2014).

An aerosol-optics model based on the RDG-FA approximation is proposed to compute the differential backscattering cross-section, i.e. the differential scattering cross-section in the backward scattering direction $\theta = \pi$, where θ is the (polar) scattering angle, and $R_g = D_g/2$, as

$$\mathrm{d}C^{\mathrm{bac}} = N^2 k^4 R_m^6 F(m) S\left(q_\pi, R_g, D_f\right), \tag{9}$$

or using the aggregate volume $V_{agg} = \frac{4}{3}\pi N R_m^3$:

$$\mathrm{d}C^{\mathrm{bac}} = 9\pi^2 \frac{V_{agg}^2}{\lambda^4} F(m) S\left(q_\pi, R_g, D_f\right), \tag{10}$$

with $q_\pi = q\,(\theta = \pi, \lambda) = 2k$ defined as the *backscattering wave-vector*. In conventional light-scattering studies, the scattering angle is varied to change q, and thus, probe different length scales (q^{-1}). Note, however, that in elastic backscatter lidar applications, where the angle is fixed at $\theta = \pi$, different length scales can still be probed by varying λ. For our lidar sensor, $q_\pi = 0.0236\,\mathrm{nm^{-1}}$ for a laser emitting at 532 nm.

An important parameter to introduce here is the backscattering structure factor $S\left(q_\pi, R_g, D_f\right)$. This factor describes the backscattered intensity in the RDG-FA approximation and has been widely used to characterize combustion byproducts. It is a dimensionless value defined as the square of the Fourier transform of the auto-correlation function, representing an aggregate's structure in reciprocal space, and can be divided into three scattering regimes (Sorensen, 2001). Several analytical expressions for $S(q)$ are available and can be used to express $S(q_\pi)$. Each expression shares the characteristic behavior of the Guinier and power-law regimes described above.

A popular expression is the one proposed by Dobbins and Megaridis (1991) as,

$$S(q_\pi) = \begin{cases} \exp\left(-\frac{q_\pi^2 R_g^2}{3}\right) & \text{if } q_\pi R_g < \sqrt{\frac{3D_f}{2}}, \\ \left(\frac{3D_f}{2e q_\pi^2 R_g^2}\right)^{-\frac{D_f}{2}} & \text{if } q_\pi R_g > \sqrt{\frac{3D_f}{2}}, \end{cases} \tag{11}$$

where $e = 2.718$. Next, due to the small size of the particulate matter emitted by the aircraft engine, the first expression will be used.

2.3 Colibri Aerosol Lidar (CAL) sensor

A novel sensor, named Colibri Aerosol Lidar (CAL), has been developed to measure nvPM concentrations in real-time with high accuracy, without sampling, directly from an aircraft engine exhaust. Different versions of the CAL instrument have been developed to address various needs and measurement scenarios (Ceolato et al., 2022, 2020). The CAL is a compact and lightweight short-range elastic backscatter lidar (SR-EBL) featuring a bi-static, multi-axial configuration, specifically designed for aerosol remote-sensing. The optical layout of the CAL sensor is shown in Fig. 1, and the main specifications are summarized in Table 1. It is capable of achieving range resolutions on the order of several tens of centimeters, together with a temporal resolution of 50 ms. The emitter unit consists of a compact, air-cooled Nd:YAG laser that emits ns pulses with a pulse energy of 20 mJ, wavelength of $\lambda = 532.8$ nm, 20 Hz, and a beam divergence of 0.5 mrad. A pair of lenses expands and collimates the laser beam before directing it toward the particulate matter, here the aircraft engine exhaust plume. The receiver unit uses a 90 mm Cassegrain telescope with a field stop to control its field of view and collect the backscattered light. Then, a collection of optical elements, including achromatic doublet (AD) lenses, a neutral-band filter (NBF), and an interference filter (IF), is placed on a translation stage to allow fine adjustment of the focal plane. This feature is crucial because it resolves focusing problems encountered for short ranges. The bi-static angle, i.e. the angle subtended between the transmitter and receiver units, is another essential feature for short-range measurements as it enables full control of the overlap function. Subsequently, the sensing unit incorporates an ultrafast photomultiplier tube (PMT). The PMT signal is digitized by a 12-bit analogue-to-digital converter (ADC) at a sampling rate of $1\,\mathrm{GS\,s^{-1}}$, then processed by a field-programmable gate array (FPGA) to extract the distance-resolved backscatter signal. The data is then transmitted to a computer for analysis and processing to determine the range-resolved backscatter signal using the Time-of-Flight (ToF) principle, which depends on the number and mass concentration, n_o and m_o respectively.

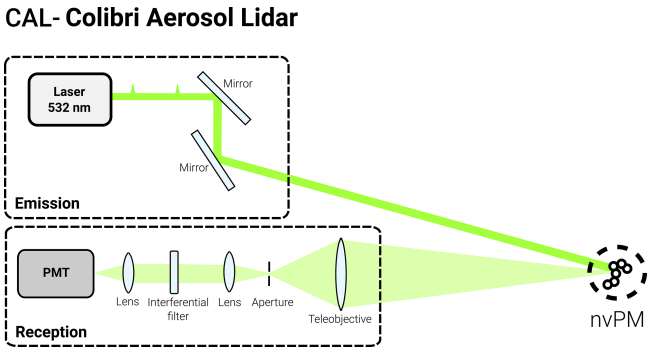

Figure 1. Optical diagram and specifications of the CAL sensor. A Nd:YAG laser along with a collimator emits a laser beam in the direction of the aerosol plume. The backscattered light is collected by a compact Cassegrain telescope then relayed by another achromatic lens to the PMT.

Table 1. Main specifications of the Colibri Aerosol Lidar (CAL) sensor.

Laser	Wavelength	532 nm
	Pulse duration	6 ns
	Pulse repetition rate	20 Hz
	Pulse energy	20 mJ
	Beam divergence	0.5 mrad
	Beam diameter	3 mm
	Bi-static angle	1–5 mrad
Receiver	Type	Cassegrain
	Effective diameter	90 mm
	Focal length	500 mm
Sensor	Type	Hamamatsu PMT
	Bandwidth	1.0 GHz
	Active area	0.2 mm^2

The salient advantages of the SR-EBL technique, which is employed by the CAL sensor, are outlined below. First, it provides a non-invasive measurement of particles, thus reducing potential errors associated with sampling. Specifically, sampling biases and contamination are two major sources of uncertainties that can significantly impact the accuracy of nvPM measurements. Second, it leverages short-range aerosol lidar technology to measure particles directly near the emission source, such as an aircraft engine, by minimizing the overlap between the laser beam and the receiver's field of view. This technique thereby bridges the gap between in situ and long-range remote sensing techniques. This innovation effectively eliminates the conventional blind zone of atmospheric aerosol lidar systems within the first 100 m. Third, it offers higher spatial and temporal resolution than other lidar sensors, enabling more precise characterization of nvPM distributions, which is critical for assessing soot emissions in a complex environment such as an airport with multiple sources of pollution. Finally, it enables high-sensitivity, range-resolved detection of aerosol particles across the entire lidar field of view, including regions in the immediate vicinity of aircraft plumes. This ensures a comprehensive characterization of particles emitted by the engine, reducing potential losses associated with sampling limitations, unlike local in situ techniques that require complex sampling apparatus and are subject to particle losses and sampling biases.

The original feature of this technique is its ability to operate directly in the exhaust plume, without contact, and without sampling or diluting the soot particles in cells. The CAL sensor has been tested during a field campaign using a turbulent kerosene Jet A-1 pool-fire and has shown promising results for measuring nvPM concentrations in real-time. The next step was to deploy the CAL sensor in an airport campaign to evaluate its performance under real-world conditions, using a commercial aircraft engine. The results of this study provide valuable information about the potential use of the CAL sensor to assess the nvPM mass and number concentration near aircraft plumes.

3 Results

The objective here is to demonstrate the feasibility of remotely measuring PM emissions using the CAL sensor based on engine thrust conditions. A brief measurement campaign was conducted, as detailed in the following sections, to evaluate the potential use of the CAL sensor to measure nvPM emissions of aircraft engines, both in terms of mass and number concentrations. This campaign aimed to further assess the performance and suitability of the sensor under real-world conditions on an airport. The data obtained during this study provide valuable insights into the future capabilities of the CAL sensor for the precise characterization of aircraft nvPM emissions.

3.1 Experimental conditions

The measurements presented in this study were collected during an experimental campaign that was conducted in February 2022 at the Airbus SAS Bikini outdoor test facility, Toulouse Blagnac Airport (IATA:TLS), France (43°38′06″ N, 1°22′04″ E). The CAL sensor proved to be both easy and practical to operate over several hours in an airport environment. The instrument was positioned at an estimated lateral distance of 47 m from the centerline of the plume and approximately 15 m from the engine exit plane. Lidar measurements were conducted along a near-horizontal trajectory using the CAL sensor positioned inside a vehicle. The laser beam was maintained at an approximate height of about 2 m above the tarmac, precisely aligned to intersect the aircraft engine plume perpendicularly. A single Rolls-Royce Trent XWB-84 engine on an Airbus A350-900 Flight Lab aircraft was operated on conventional Jet A-1 fuel.

Figure 2. Picture of the test setup at the Airbus SAS Bikini outdoor test facility with an Airbus A350-900 Flight Lab test aircraft. The arrows indicate the location of the CAL sensor and a beam stop for laser safety.

3.2 Calibration

A significant challenge in conducting short-range lidar measurements is the incomplete overlap between the lidar's transmitter and receiver. This overlap issue is a key cause of uncertainty when profiling the radiative and microphysical properties of aerosols using short-range lidars. This can be viewed as a variation in the image-plane position that depends on the range to the scattering volume, which directly impacts the lidar's collection efficiency. Consequently, backscattered light in the short-range may not fully reach the optical sensor. This area is commonly known as the lidar incomplete overlap or blind zone. Despite numerous techniques proposed to determine the overlap function of lidar systems (Halldórsson and Langerholc, 1978; Harms, 1979; Sasano et al., 1979; Dho et al., 1997; Wandinger and Ansmann, 2002; Guerrero-Rascado et al., 2010; Vande Hey et al., 2011; Biavati et al., 2011; Li et al., 2016), experimental approaches are often preferred due to the lack of accurate lidar specifications required for theoretical methods. The CAL sensor features a bi-static, multi-axial design that is specifically optimized to profile aerosols in the short-range while minimizing the incomplete overlap zone. A measurement of the range-dependent overlap function was performed using a Lambertian surface, as detailed in (Ceolato et al., 2020), to confirm that full overlap was achieved after 30 m.

3.3 Aircraft nvPM measurements

In the following, the nvPM mass and number concentrations are derived from volume backscatter coefficients measured by our CAL sensor. Such backscatter measurements can be converted to mass concentrations by dividing them by a reference mass backscatter coefficient (MBC; units of $m^2\,g^{-1}\,sr^{-1}$) and number concentrations by dividing them by a reference differential backscatter cross-section (dC^{bac}; units of $m^2\,sr^{-1}$), following Eqs. (6) and (4) respectively. This data processing is similar to the one commonly used in optical techniques such as LII, CAPS, or PAX and also relies on a reference coefficient, although here the measurand is not incandescence or absorption but backscattering. The reference MBC used here to report nvPM represents an assumed physical property of the nvPM emitted by the engine at a given time. In this study, we have used the value of $MBC = 0.025\,m^2\,g^{-1}\,sr^{-1}$ and $dC^{bac} = 1.38\,nm^2\,sr^{-1}$, which is provided by the backscattering RDG-FA model, described in Sect. 2.2.

During the test, a series of lidar measurements were performed under various engine thrust conditions. An adaptive PMT gain was employed to optimize the signal-to-noise ratio while avoiding saturation of the CAL sensor from ambient illumination; once adjusted, the gain was fixed for the entire measurement. The recorded lidar signals were background-corrected and time-averaged following usual lidar procedures. Clear-air background profiles were used to remove ambient aerosol contributions, ensuring that the resulting backscatter is solely attributed to soot particles emitted by the engine. The volume backscatter profiles were then derived from these raw signals using the analysis methodology outlined in Sect. 2.1.

Figure 3 presents a time-range false-color map of the volume backscatter coefficient (left) of an initial measurement test and the retrieved nvPM mass and number concentration profiles (right). The left panel reveals temporal and spatial variations in backscattering, with a distinctly high backscatter coefficient at the engine exhaust location. In particular, particles are clearly detected from background aerosols with a volume backscatter coefficient greater than $10^{-6}\,m^{-1}\,sr^{-1}$. The right panel shows the time-averaged, over a 3 min period, horizontal distributions of nvPM mass and number concentrations, peaking at the engine location and forming an almost perfect Gaussian plume of about 6 m. The presence of

Table 2. Mass and number concentrations obtained from the CAL sensor at various engine thrust conditions. Maximum and standard deviation values.

Engine thrust	Mass $[\mathrm{mg\,m^{-3}}]$	Number $[10^6\,\mathrm{part\,cm^{-3}}]$
Intermediate	0.081 ± 0.018	1.47 ± 0.33
High	0.055 ± 0.014	0.99 ± 0.25
Idle	0.040 ± 0.009	0.72 ± 0.16

a crosswind during the measurement caused fluctuations in the volume backscatter profiles during the measurements. Although wind fluctuations were identified, they primarily affected the standard deviation of the Gaussian plume retrieval while having negligible influence on its mean, as evidenced in the derived mass and number concentrations.

Figure 4 complements the previous analysis by illustrating a time-range map of the volume backscatter coefficient (top panel) and the retrieved nvPM mass and number concentration profiles (bottom panel) under three engine thrust conditions: intermediate, high, and ground idle. It is important to note that the measurement duration at high power was relatively brief compared to the longer periods recorded at intermediate power and idle power. The maximum mean and standard deviation values are reported in Table 2 for the mass and number concentration of nvPM. This result provides valuable insights into the temporal and spatial variations of nvPM emissions, with the CAL sensor effectively quantifying the changes in the number and mass concentration corresponding to various engine thrust levels. Table 2 presents a comprehensive summary of the nvPM mass and number concentrations using the CAL sensor. It clearly demonstrates a correlation between engine power and particulate emissions. The observed tendencies align with trends reported in the ICAO Aircraft Engine Emissions Databank (International Civil Aviation Organization, 2025), showing a non-linear relationship between engine thrust and emission levels: intermediate thrust produces the highest concentrations, followed by slightly lower values at high thrust, while idle conditions exhibit the lowest emissions. Interestingly, the concentrations do not exhibit a linear increase with thrust, showing a slight reduction at higher thrust levels. This suggests complex interactions between engine parameters and particulate formation. Recent field measurements revealed that lubrication oil could contribute to the particulate matter in near-idle exhaust plumes (Fushimi et al., 2019; Yu et al., 2012; Ungeheuer et al., 2021). These findings underscore the importance of considering specific engine operating conditions when assessing aircraft particulate emissions for standard JET A-1 and Sustainable Alternative Fuels (SAF) (Durdina et al., 2021).

4 Discussion

The development of new measurement technologies is needed to quantify non-CO_2 emissions, such as nvPM or contrails, which create complex climate impacts that cannot be addressed by traditional characterization methods alone. We propose to discuss several uncertainties and limitations, as well as potential developments to enhance the performance of the CAL sensor.

4.1 Uncertainties and limitations

Assessing uncertainties is a critical part in the development of any novel measurement method. Our analysis of the retrieval method reveals that one of the primary sources of uncertainty lies in the limited knowledge of the backscattering properties of particulate matter (PM) emitted by aircraft. To address this, an aerosol-optics model was introduced in Sect. 2.2, based on the following key equations:

$$\mathrm{d}C^{\mathrm{bac}} = 9\pi^2 \frac{V_{\mathrm{agg}}^2}{\lambda^4} F(m) S(q_\pi), \tag{12}$$

$$\mathrm{MBC} = \frac{\mathrm{d}C_{\mathrm{agg}}^{\mathrm{bac}}}{\rho V_{\mathrm{agg}}} = 9\pi^2 \frac{V_{\mathrm{agg}}}{\rho \lambda^4} F(m) S(q_\pi). \tag{13}$$

In light-scattering models, uncertainties in optical properties (e.g. refractive index) and morphological characteristics (e.g. fractal dimension, ratio of monomer radius to radius of gyration) can introduce substantial errors in the predicted backscattering behavior. To quantify the impact of these uncertainties on backscattering properties, we employ a Monte Carlo (MC) uncertainty analysis. This method involves generating a large number of random samples from the probability distributions of the input parameters, as summarized in Table 3, and evaluating the measurement model for each set of samples. The resulting distribution of output values enables the estimation of both the best value and its associated uncertainty.

Figure 5 displays the sensitivity analysis, with C^{bac} results in the upper panel and MBC results in the lower panel. The analysis uses a one-at-a-time (OAT) method and employs Pearson correlation coefficients to measure how each input variable affects outcomes across the entire ensemble of simulations. The scatter plots display linear regression lines, and the fit quality is evaluated using the Root Mean Squared Error (RMSE) and the coefficient of determination (R^2). The R^2 values indicate that the investigated parameters have a substantial and variable impact on both C^{bac} and MBC, with explained variances of 78 % and 81 %, respectively.

The other variables that showed a moderate positive linear correlation, with R^2 values around 25 %, are D_{f} and k_0 for both C^{bac} and MBC, while the only variable that exhibited an anti-correlation trend is X_{R}, with $R^2 = 26\,\%$. Lastly, $F(m)$ exhibits a weaker but still notable linear influence on both MBC and C^{bac}, although the magnitudes differ. The linear relationship between MBC and $F(m)$ accounts for a moderate

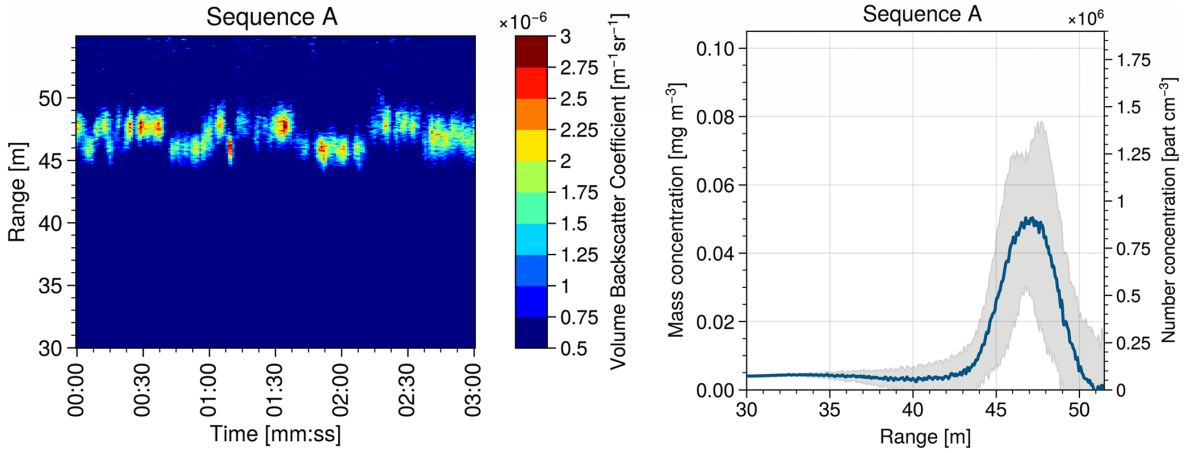

Figure 3. Time-range map of the volume backscatter coefficient (left). Retrieved nvPM mass and number concentration profiles.

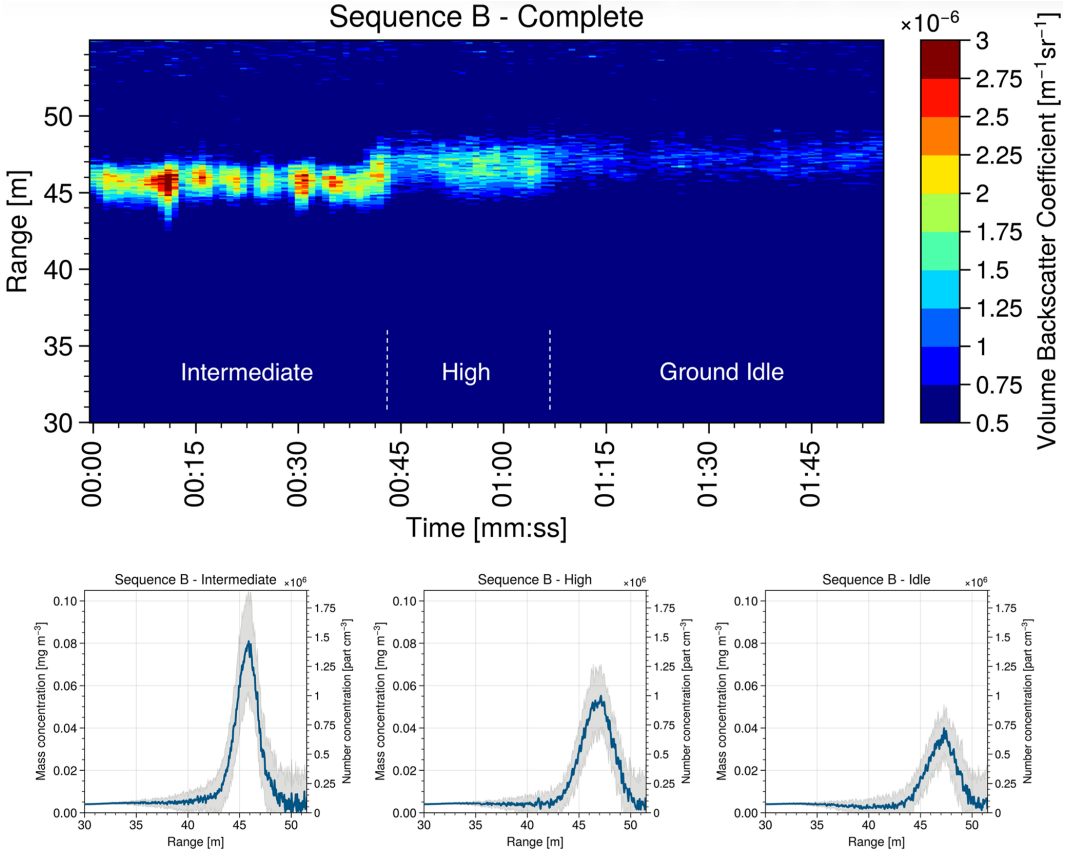

Figure 4. Time-range map of the volume backscatter coefficient (top) and retrieved nvPM mass and number concentration profiles (bottom) under three engine thrust conditions: intermediate, high, and idle.

R^2 of 33 %, while the relationship between C^{bac} and $F(m)$ is substantially weaker, with an R^2 of only 16 %. This indicates that while both parameters show some positive linear correlation with $F(m)$, MBC is more sensitive to variations in $F(m)$ than C^{bac}. In contrast, $S(q_\pi)$ shows a negligible linear correlation with MBC and C^{bac}. This suggests that linear variations in $S(q_\pi)$ have no substantial effect on C^{bac} or MBC in the framework of this analysis. It should be emphasized that this conclusion relies solely on linear regression. Therefore, depending on the analytical expression for $S(q_\pi)$ presented in Eq. (11), additional nonlinear relationships may emerge,

Table 3. Uncertainty components associated with optical properties and morphological properties of the backscattering model.

Components	Symbols	Units	Value	Uncertainty	Cback (% Var)	MBC (% Var)
Fractal dimension	D_f		1.9	±0.1	6.8	5.6
Fractal pre-factor	k_o		2.3	±0.2	6.3	5.1
D_m/D_g	X_R		0.40	±0.02	7.3	6.0
Monomer radius	R_m	nm	10.0	±1	76.2	62.0
Scattering function	$F(m)$		0.4	±0.05	3.4	11.2
Backscattering Structure Factor	$S(q_\pi)$		0.89	±0.01	0.0	0.1
Effective mass density	ρ	kg m^{-3}	1000	±100	n/a	10.0

n/a: not applicable.

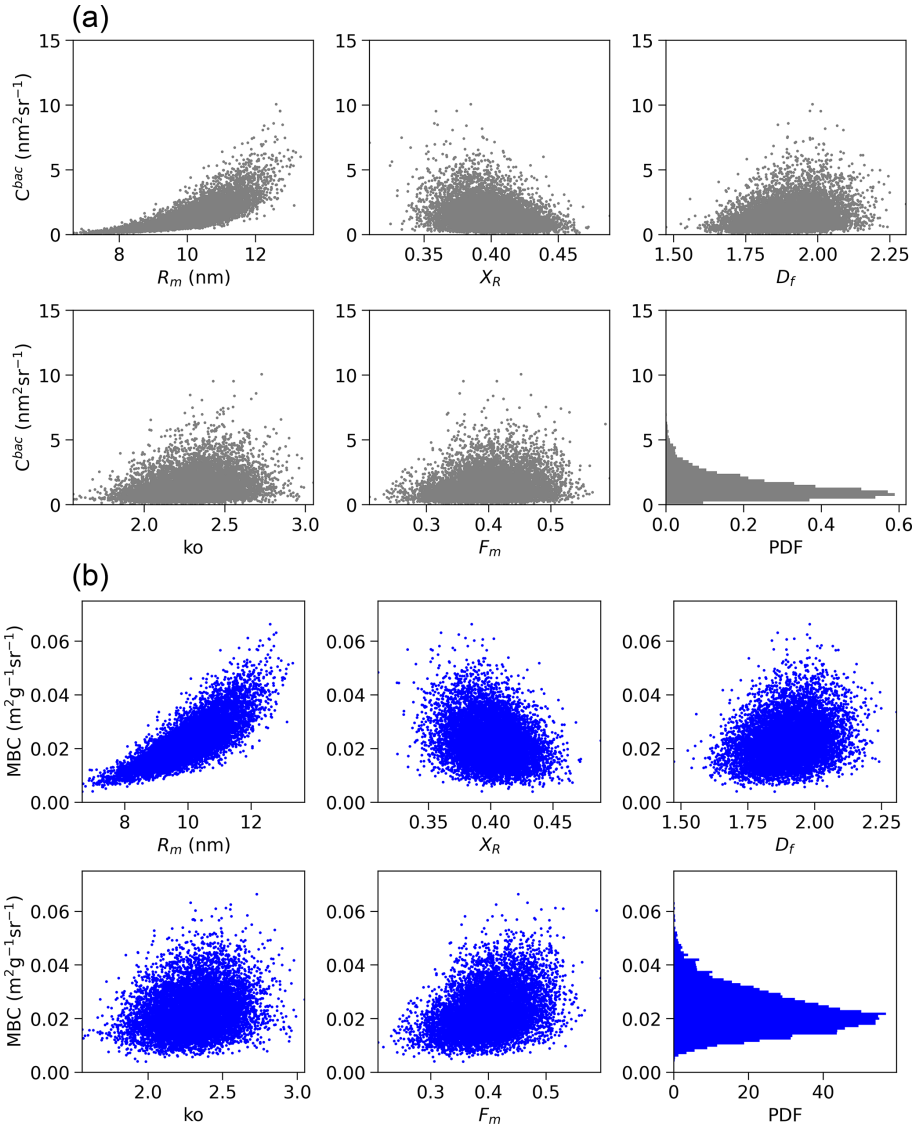

Figure 5. The results of the sensitivity analysis, based on 10 000 Monte Carlo simulations, are displayed. Each panel illustrates how individual parameters affect the variability of C^{bac} and MBC. The power density functions (PDFs) for C^{bac} and MBC are shown in the final figure of each panel. **(a)** Sensitivity analysis of (C^{bac}) with respect to key input parameters. **(b)** Sensitivity analysis of MBC with respect to key input parameters.

suggesting that new possible nonlinearities might exist beyond the scope of this linear analysis.

Based on the input data summarized in Table 3, the results of the Monte Carlo simulation – performed with 10 000 samples drawn from normal distributions – yield a mean value of $C^{\mathrm{bac}} = 1.4 \pm 1\,\mathrm{nm^2\,sr^{-1}}$, and a mean MBC of $(2.1 \pm 0.8) \times 10^{-2}\,\mathrm{m^2\,g^{-1}\,sr^{-1}}$. The histograms in Fig. 5 illustrate the output distributions, with each probability density function (PDF) normalized so that the area under the curve sums to one. Notably, Eqs. (12) and (13) display nonlinear behavior, meaning the influence of each variable on the properties of interest cannot be fully described by linear relationships alone. To evaluate the contribution of each variable, we expressed Eq. (12) in logarithmic form and then quantified the variance associated with each term as follows:

$$\log C^{\mathrm{bac}} = \log A + 2\log V_{\mathrm{agg}} + \log S(q_\pi) + \log F_{\mathrm{m}}. \tag{14}$$

Operating with Eqs. (8) and (9) the following explicit form of V_{agg} is used

$$V_{\mathrm{agg}} = \frac{4}{3}\pi\, k_0\, R_{\mathrm{m}}^3 \left(X_{\mathrm{R}}^{-1}\right)^{D_{\mathrm{f}}} \tag{15}$$

Equation (15) can be reformulated by combining the resulting terms as follows,

$$\begin{aligned}\log C^{\mathrm{bac}} &= \log A + 2\left(\log k_{\mathrm{o}} + 3\log R_{\mathrm{m}} + D_{\mathrm{f}}\log\left(X_{\mathrm{R}}^{-1}\right)\right) \\ &\quad + \log S(q_\pi) + \log F_{\mathrm{m}}.\end{aligned} \tag{16}$$

Similarly, Eq. (13) is decomposed for MBC as follows,

$$\begin{aligned}\log \mathrm{MBC} &= \log k_{\mathrm{o}} + 3\log R_{\mathrm{m}} + D_{\mathrm{f}}\log\left(X_R^{-1}\right) + \log S(q_\pi) \\ &\quad + \log F_{\mathrm{m}} - \log\rho + B,\end{aligned} \tag{17}$$

where $A = 9\pi^2/\lambda^4$ and B represents the unit conversion for MBC.

The variable apportionment results are summarized in the last two columns of Table 3. In brief, R_{m} is the most influential variable for C_{bac}, explaining up to 76.2 % of the variance for C_{bac} and 62 % for MBC. The contributions from all other variables remain below 13 % for both C_{bac} and MBC. This analysis further reveals that the variance of V_{agg} explains up to 96.6 % of the variability in C_{bac}, and 87.9 % in MBC.

4.2 Further development

This study introduces the CAL sensor, which was successfully deployed to measure nvPM emissions from the exhaust of an Airbus A350-900 Flight Lab aircraft engine. The sensor demonstrated high performance in real-time monitoring, providing critical insights into soot properties and behavior across a range of engine operating conditions. Results confirmed its ability to accurately quantify nvPM mass and number concentrations, thereby validating its effectiveness for characterizing aircraft exhaust. These findings highlight the potential of the CAL sensor to advance aerosol science, atmospheric research, and emission monitoring in the aviation sector, offering novel opportunities to improve regulatory compliance and environmental impact assessments.

Compared to the concentrations reported by ICAO, our dataset exhibits low measurement uncertainties, reinforcing the reliability of the aerosol optical model used to characterize aircraft PM emissions. This gives us confidence in the model's ability to reproduce key optical properties under realistic engine operating conditions. However, comparing emissions data from different measurement platforms remains challenging due to variability introduced by particle dilution in the engine exhaust plume. The dilution factor, which is governed by ambient conditions, distance from the exhaust, and plume mixing dynamics, can substantially alter the observed particle concentration. Further work should include a direct comparison between in situ measurements obtained near the engine exit plane and remote-sensing observations, such as lidar measurements taken further downwind. Accurate quantification of dilution effects is critical for enabling rigorous comparisons and model validation across diverse spatial and temporal measurement conditions.

Future research should also address the formation and evolution of vPM. Lidar techniques stand out by enabling measurements across the exhaust plume, from the engine exit plane to downstream regions where vPM forms due to cooling and condensation. This capability not only refines traditional in-situ sampling but also enables a more complete characterization of total particulate matter (tPM), which includes both nvPM and vPM. Another key challenge is assessing particulate matter emission-indices from lidar measurements by integrating engine performance data, such as fuel flow rates or carbon dioxide concentrations, in accordance with ICAO emission-index standards. Bridging this gap would mark a significant advancement in standardizing the quantification of aircraft emissions.

5 Conclusion

Aircraft engine emissions are a pressing environmental and public health concern due to their role in degrading air quality around airports and their contribution to contrail formation, which impacts climate. The development of novel techniques to measure these emissions supports efforts to reduce aviation's environmental footprint and provides valuable insights for policies promoting sustainable air transport. This work introduces a non-invasive approach for measuring aircraft engine particulate emissions, offering a breakthrough by enabling rapid, accurate, and remote assessments without the logistical constraints of direct sampling. The method combines short-range elastic backscatter lidar measurements with a backscattering model for nvPM emissions of engine exhausts. We deployed our compact and field-deployable lidar system, named CAL sensor, to measure the PM emis-

sions of an aircraft engine at Toulouse Airport. Field results confirmed the sensor's ability to reliably capture backscatter profiles of PM across various thrust levels. By applying a soot backscattering model, we inverted these measurements to determine both number and mass concentrations. Overall, these findings highlight the CAL sensor's potential as a flexible and robust solution for quantifying aircraft PM emissions. The use of the CAL sensor could enhance the quantification of particulate matter emissions in real operational conditions. This advancement addresses key challenges in air quality monitoring and supports regulatory efforts toward emission reduction, contributing to the aviation decarbonization roadmap through improved assessment of sustainable aviation fuels (SAFs) and emerging engine technologies. The method's successful validation at a major European test site not only strengthens its credibility but also paves the way for industry-wide adoption as a scalable solution. In summary, our findings represent a significant step forward in environmental monitoring technology, with tangible benefits for science, policy, and society.

Code availability. The code used for data processing is not publicly available at this time, as it is part of proprietary ONERA software. Requests for access can be directed to the corresponding author.

Data availability. The raw measurement data presented in this study were collected during a proprietary Airbus test campaign and are subject to confidentiality agreements. Processed data supporting the findings may be made available upon reasonable request to the corresponding author, subject to approval by the data owners.

Author contributions. RC developed the instrument and the methodology, with support from ABV, GL, LG, AV, IO, and DD. The data were analyzed and processed by ABV and RC. RC drafted the manuscript, with contributions and revisions from ABV and CR. The experimental trials were initiated and coordinated by PL, CR, KS, and MJ. The structure and scope of the paper were defined collaboratively by all the authors.

Competing interests. The contact author has declared that none of the authors has any competing interests.

Disclaimer. Publisher's note: Copernicus Publications remains neutral with regard to jurisdictional claims made in the text, published maps, institutional affiliations, or any other geographical representation in this paper. The authors bear the ultimate responsibility for providing appropriate place names. Views expressed in the text are those of the authors and do not necessarily reflect the views of the publisher.

Acknowledgements. The authors express their sincere gratitude to the individuals and organizations whose contributions were invaluable to this research. We thank Prof. Jerome Yon, Prof. Matthew J. Berg, and Prof. Chris Sorensen for their expert advice on soot characterization and light-scattering models. Our appreciation extends to the Airbus Flight-Lab team for their support in conducting lidar measurements and providing access to test facilities. We are grateful to Gauthier Le Chenadec, Maxime Gauthier, and Abhijeet Sanjay Badhe for their assistance and contributions. The ongoing development, production, assessment, and analysis of CAL instrument and data are supported by ONERA. We acknowledge the Direction Générale de l'Aviation Civile (DGAC), ONERA's Direction Scientifique Générale (DSG), and Direction Programme Aéronautique (DPA) for their scientific guidance and resources that were crucial for this research. This work would not have been possible without their collective expertise and support.

Financial support. This research has been supported by the Office National d'études et de Recherches Aérospatiales (grant nos. PRF OPSIDIA and PRF PROMETE).

Review statement. This paper was edited by Cuiqi Zhang and reviewed by two anonymous referees.

References

Aamaas, B., Lund, M. T., Fuglestvedt, J. S., Totterdill, A., Owen, B., Skowron, A., and Lee, D. S.: Continued global warming from aviation even under high-ambition mitigation scenarios, One Earth, 8, 101451, https://doi.org/10.1016/j.oneear.2025.101451, 2025.

Bedoya-Velásquez, A. E., Ceolato, R., Titos, G., Bravo-Aranda, J. A., Casans, A., Patrón, D., Fernández-Carvelo, S., Guerrero-Rascado, J. L., and Alados-Arboledas, L.: Synergy between Short-Range Lidar and In Situ Instruments for Determining the Atmospheric Boundary Layer Lidar Ratio, Remote Sensing, 16, https://doi.org/10.3390/rs16091583, 2024.

Biavati, G., Di Donfrancesco, G., Cairo, F., and Feist, D. G.: Correction scheme for close-range lidar returns, Appl. Optics, 50, 5872–5882, https://doi.org/10.1364/AO.50.005872, 2011.

Ceolato, R. and Berg, M. J.: Aerosol light extinction and backscattering: A review with a lidar perspective, J. Quant. Spectrosc. Ra., 262, 107492, https://doi.org/10.1016/j.jqsrt.2020.107492, 2021.

Ceolato, R., Bedoya-Velásquez, A. E., and Mouysset, V.: Short-Range Elastic Backscatter Micro-Lidar for Quantitative Aerosol Profiling with High Range and Temporal Resolution, Remote Sensing, 12, https://doi.org/10.3390/rs12203286, 2020.

Ceolato, R., Bedoya-Velasquez, A., Fossard, F., Mouysset, V., Paulien, L., Lefebvre, S., Mazzoleni, C., Sorensen, C., Berg, M., and Yon, J.: Black carbon aerosol number and mass concentration measurements by picosecond short-range elastic backscatter lidar, Scientific Reports, 12, 8443, https://doi.org/10.1038/s41598-022-11954-7, 2022.

Ceolato, R., Yon, J., and Berg, M. J.: Lidar backscattering model for soot aerosols, J. Quant. Spectrosc. Ra., 345, 109532, https://doi.org/10.1016/j.jqsrt.2025.109532, 2025.

Delhaye, D., Ouf, F.-X., Ferry, D., Ortega, I. K., Penanhoat, O., Peillon, S., Salm, F., Vancassel, X., Focsa, C., Irimiea, C., Harivel, N., Perez, B., Quinton, E., Yon, J., and Gaffie, D.: The MERMOSE project: Characterization of particulate matter emissions of a commercial aircraft engine, J. Aerosol Sci., 105, 48–63, https://doi.org/10.1016/j.jaerosci.2016.11.018, 2017.

Dho, S. W., Park, Y. J., and Kong, H. J.: Experimental determination of a geometric form factor in a lidar equation for an inhomogeneous atmosphere, Appl. Optics, 36, https://doi.org/10.1364/ao.36.006009, 1997.

Digby, R. A. R., von Salzen, K., Monahan, A. H., Gillett, N. P., and Li, J.: The impact of uncertainty in black carbon's refractive index on simulated optical depth and radiative forcing, Atmos. Chem. Phys., 25, 3109–3130, https://doi.org/10.5194/acp-25-3109-2025, 2025.

Dobbins, R. A. and Megaridis, C. M.: Absorption and scattering of light by polydisperse aggregates, Appl. Optics., 30, 4747–4754, https://doi.org/10.1364/AO.30.004747, 1991.

Durand, E., Durdina, L., Smallwood, G., Johnson, M., Spirig, C., Edebeli, J., Roth, M., Brem, B., Sevcenco, Y., and Crayford, A.: Correction for particle loss in a regulatory aviation nvPM emissions system using measured particle size, J. Aerosol Sci., 169, 106140, https://doi.org/10.1016/j.jaerosci.2023.106140, 2023.

Durdina, L., Brem, B., Abegglen, M., Lobo, P., Rindlisbacher, T., Thomson, K., Smallwood, G., Hagen, D., Sierau, B., and Wang, J.: Determination of PM mass emissions from an aircraft turbine engine using particle effective density, Atmos. Environ., 99, 500–507, https://doi.org/10.1016/j.atmosenv.2014.10.018, 2014.

Durdina, L., Brem, B. T., Elser, M., Schönenberger, D., Siegerist, F., and Anet, J. G.: Reduction of Nonvolatile Particulate Matter Emissions of a Commercial Turbofan Engine at the Ground Level from the Use of a Sustainable Aviation Fuel Blend, Environ. Sci. Technol., 55, 14576–14585, https://doi.org/10.1021/acs.est.1c04744, 2021.

Fushimi, A., Saitoh, K., Fujitani, Y., and Takegawa, N.: Identification of jet lubrication oil as a major component of aircraft exhaust nanoparticles, Atmos. Chem. Phys., 19, 6389–6399, https://doi.org/10.5194/acp-19-6389-2019, 2019.

Guerrero-Rascado, J. L., Costa, M. J., Bortoli, D., Silva, A. M., Lyamani, H., and Alados-Arboledas, L.: Infrared lidar overlap function: an experimental determination, Opt. Express, 18, 20350–20369, https://doi.org/10.1364/OE.18.020350, 2010.

Halldórsson, T. and Langerholc, J.: Geometrical form factors for the lidar function, Appl. Optics, 17, https://doi.org/10.1364/ao.17.000240, 1978.

Harms, J.: Lidar return signals for coaxial and noncoaxial systems with central obstruction, Appl. Optics, 18, 1559–66, https://doi.org/10.1364/AO.18.001559, 1979.

ICAO: Annex 16 to the Convention on International Civil Aviation: Environmental Protection, Volume II – Aircraft Engine Emissions, ICAO, 4th edn., ISBN 978-92-9258-358-4, 2017.

International Civil Aviation Organization: ICAO Aircraft Engine Emissions Databank, https://www.easa.europa.eu/en/domains/environment/icao-aircraft-engine-emissions-databank (last access: 1 February 2025), 2025.

Ishimoto, H., Kudo, R., and Adachi, K.: A shape model of internally mixed soot particles derived from artificial surface tension, Atmos. Meas. Tech., 12, 107–118, https://doi.org/10.5194/amt-12-107-2019, 2019.

Jones, S. H. and Miake-Lye, R. C.: Parameterization of H2SO4 and organic contributions to volatile PM in aircraft plumes at ground idle, J. Air Waste Manage., 74, 490–510, https://doi.org/10.1080/10962247.2024.2354820, 2024.

Kanngiesser, F. and Kahnert, M.: Coating material-dependent differences in modelled lidar-measurable quantities for heavily coated soot particles, Opt. Express, 27, 36368–36387, https://doi.org/10.1364/OE.27.036368, 2019.

Klöwer, M., Allen, M. R., Lee, D. S., Proud, S. R., Gallagher, L., and Skowron, A.: Quantifying aviation's contribution to global warming, Environ. Res. Lett., 16, 104027, https://doi.org/10.1088/1748-9326/ac286e, 2021.

Kumal, R. R., Liu, J., Gharpure, A., Vander Wal, R. L., Kinsey, J. S., Giannelli, B., Stevens, J., Leggett, C., Howard, R., Forde, M., Zelenyuk, A., Suski, K., Payne, G., Manin, J., Bachalo, W., Frazee, R., Onasch, T. B., Freedman, A., Kittelson, D. B., and Swanson, J. J.: Impact of Biofuel Blends on Black Carbon Emissions from a Gas Turbine Engine, Energ. Fuel., 34, 4958–4966, https://doi.org/10.1021/acs.energyfuels.0c00094, 2020.

Lee, D. S., Allen, M. R., Cumpsty, N., Owen, B., Shine, K. P., and Skowron, A.: Uncertainties in mitigating aviation non-CO2 emissions for climate and air quality using hydrocarbon fuels, Environ. Sci.: Atmos., 3, 1693–1740, https://doi.org/10.1039/D3EA00091E, 2023.

Li, J., Li, C., Zhao, Y., Li, J., and Chu, Y.: Geometrical constraint experimental determination of Raman lidar overlap profile, Appl. Optics, 55, 4924–4928, https://doi.org/10.1364/AO.55.004924, 2016.

Liu, F., Yon, J., Fuentes, A., Lobo, P., Smallwood, G. J., and Corbin, J. C.: Review of recent literature on the light absorption properties of black carbon: Refractive index, mass absorption cross section, and absorption function, Aerosol Sci. Tech., 54, 33–51, https://doi.org/10.1080/02786826.2019.1676878, 2020.

Liu, L. and Mishchenko, M. I.: Spectrally dependent linear depolarization and lidar ratios for nonspherical smoke aerosols, J. Quant. Spectrosc. Ra., 248, 106953, https://doi.org/10.1016/j.jqsrt.2020.106953, 2020.

Marhaba, I., Ferry, D., Laffon, C., Regier, T. Z., Ouf, F.-X., and Parent, P.: Aircraft and MiniCAST soot at the nanoscale, Combust. Flame, 204, 278–289, https://doi.org/10.1016/j.combustflame.2019.03.018, 2019.

Measures, R. M.: Laser remote sensing: Fundamentals and applications, New York, Wiley-Interscience, 1984.

Mishchenko, M. I., Travis, L. D., and Lacis, A. A.: Scattering, absorption, and emission of light by small particles, Cambridge University Press, 2002.

Moteki, N., Ohata, S., Yoshida, A., and Adachi, K.: Constraining the complex refractive index of black carbon particles using the complex forward-scattering amplitude, Aerosol Sci. Tech., 57, 678–699, https://doi.org/10.1080/02786826.2023.2202243, 2023.

Qin, Z., Wang, H., He, A., Sun, Y., Li, J., Zhang, Y., and Zhang, Q.: Backscattering Linear Depolarization Ratio of Smoke Aerosols From Biomass Burning, J. Geophys. Res.-Atmos., 129, e2024JD041276, https://doi.org/10.1029/2024JD041276, 2024.

SAE International: Procedure for the Continuous Sampling and Measurement of Non-Volatile Particulate Matter Emissions from Aircraft Turbine Engines, Aerospace Recommended Practice ARP6320, SAE International, https://doi.org/10.4271/ARP6320, 2018.

SAE International: Procedure for the Calculation of Non-Volatile Particulate Matter Sampling and Measurement System Losses and System Loss Correction Factors, Aerospace Recommended Practice ARP6481, SAE International, https://doi.org/10.4271/ARP6481, 2019.

Sasano, Y., Shimizu, H., Takeuchi, N., and Okuda, M.: Geometrical form factor in the laser radar equation: an experimental determination, Appl. Optics, 18, 3908–10, https://doi.org/10.1364/AO.18.003908, 1979.

Smith, A. J. A., Peters, D. M., McPheat, R., Lukanihins, S., and Grainger, R. G.: Measuring black carbon spectral extinction in the visible and infrared, J. Geophys. Res.-Atmos., 120, 9670–9683, https://doi.org/10.1002/2015JD023564, 2015.

Sorensen, C. M.: Light Scattering by Fractal Aggregates: A Review, Aerosol Sci. Tech., 35, 648–687, https://doi.org/10.1080/02786820117868, 2001.

Teoh, R., Stettler, M. E., Majumdar, A., Schumann, U., Graves, B., and Boies, A. M.: A methodology to relate black carbon particle number and mass emissions, J. Aerosol Sci., 132, 44–59, https://doi.org/10.1016/j.jaerosci.2019.03.006, 2019.

Trivanovic, U., Kelesidis, G. A., and Pratsinis, S. E.: High-throughput generation of aircraft-like soot, Aerosol Sci. Tech., 56, 732–743, https://doi.org/10.1080/02786826.2022.2070055, 2022.

Ungeheuer, F., van Pinxteren, D., and Vogel, A. L.: Identification and source attribution of organic compounds in ultrafine particles near Frankfurt International Airport, Atmos. Chem. Phys., 21, 3763–3775, https://doi.org/10.5194/acp-21-3763-2021, 2021.

Vande Hey, J., Coupland, J., Foo, M. H., Richards, J., and Sandford, A.: Determination of overlap in lidar systems, Appl. Optics, 50, 5791–5797, https://doi.org/10.1364/AO.50.005791, 2011.

Wandinger, U. and Ansmann, A.: Experimental determination of the lidar overlap profile with Raman lidar, Appl. Optics, 41, 511–514, https://doi.org/10.1364/ao.41.000511, 2002.

Yu, F., Kärcher, B., and Anderson, B. E.: Revisiting Contrail Ice Formation: Impact of Primary Soot Particle Sizes and Contribution of Volatile Particles, Environ. Sci. Technol., 58, 17650–17660, https://doi.org/10.1021/acs.est.4c04340, 2024.

Yu, Z., Herndon, S. C., Ziemba, L. D., Timko, M. T., Liscinsky, D. S., Anderson, B. E., and Miake-Lye, R. C.: Identification of Lubrication Oil in the Particulate Matter Emissions from Engine Exhaust of In-Service Commercial Aircraft, Environ. Sci. Technol., 46, 9630–9637, https://doi.org/10.1021/es301692t, 2012.